Theoretical and Applied Fracture Mechanics 70 (2014) 1–9

Contents lists available at ScienceDirect

Theoretical and Applied Fracture Mechanics

journal homepage: www.elsevier.com/locate/tafmec

Structure of micro-crack population and damage evolution in quasi-brittle media

Andrey P. Jivkov *

Mechanics and Physics of Solids Research Team, School of Mechanical, Aerospace and Civil Engineering, The University of Manchester, Oxford Road, Manchester M13 9PL, UK

ARTICLE INFO

Article history:
Available online 19 April 2014

Keywords:
Quasi-brittle material
Lattice model
Defect distribution
Crack population
Macroscopic damage

ABSTRACT

Mechanical behaviour of quasi-brittle materials, such as concrete and rock, is controlled by the generation and growth of micro-cracks. A 3D lattice model is used in this work for generating micro-crack populations. In the model, lattice sites signify solid-phase blocks and lattice bonds transmit forces and moments between adjacent sites. Micro-cracks are generated at the interfaces between solid-phase blocks, where initial defects are allocated according to given size distribution. This is represented by removal of bonds when a criterion based on local forces and defect size is met. The growing population of micro-cracks results in a non-linear stress–strain response, which can be characterised by a standard damage parameter. This population is analysed using a graph-theoretical approach, where graph nodes represent failed faces and graph edges connect neighbouring failed faces, i.e. coalesced micro-cracks. The evolving structure of the graph components is presented and linked to the emergent non-linear behaviour and damage. The results provide new insights into the relation between the topological structure of the population of micro-cracks and the material macroscopic response. The study is focused on concrete, for which defect sizes were available, but the proposed methodology is applicable to a range of quasi-brittle materials with similar dominant damage mechanisms.

1. Introduction

The mechanical behaviour of quasi-brittle materials, such as concrete, graphite, ceramics, or rock, emerges from underlying microstructure changes. The meaning of microstructure differs for different media and could be characterised by intrinsic length scales. For concrete these could be aggregate sizes and inter-aggregate distances, while for rock systems these could be sizes of blocks formed between existing small fractures. At the engineering length scale, orders of magnitude larger than the microstructure scales, the mechanical behaviour can be described with continuum constitutive laws of increasing complexity combining damage, plasticity and time-dependent effects [1–4]. In these phenomenological approaches damage represents reduction of the material elastic constants. From microstructure length scale perspective damage in quasi-brittle media is introduced by nucleation and evolution of micro-cracks, where a micro-crack means a fracture of the order of the microstructure scale(s). Potentially the effect of the micro-cracks formed under loading could be captured by continuum damage models calibrated against engineering scale experiments. The phenomenology, however, cannot help to understand the effects of the generated micro-crack population on other important physical properties of the material. In many applications the quasi-brittle materials have additional functions as barriers to fluid transport via convection, advection, and/or diffusion. It is therefore important to take a mechanistic view on the development of damage by modelling the evolution of micro-crack population. This can inform us about changes in the transport properties. Such a mechanistic approach needs to account for the microstructure in a way corresponding to the micro-crack formation mechanism [5]. In concrete, micro-cracks typically emerge from pores in the interfacial transition zone between the cement paste and aggregates [6]. In rock systems, micro-crack generating features could be existing fractures as well as pores. Concrete will be used in this work to demonstrate the proposed methodology, because data for the micro-crack initiating features in this material is readily available.

Discrete lattice representation of the material microstructure seems to offer the most appropriate modelling strategy for analysis of micro-crack populations. Discrete lattices allow for studies of distributed damage without constitutive assumptions about crack paths and coalescence that would be needed in a continuum finite element modelling. For lattice construction, the material is

* Tel.: +44 (0) 161 306 3765.
E-mail address: andrey.jivkov@manchester.ac.uk

http://dx.doi.org/10.1016/j.tafmec.2014.04.003
0167-8442/

appropriately subdivided into cells and lattice sites are placed at the cell centres. The deformation of the represented continuum arises from interactions between the lattice sites. These involve forces resisting relative displacements and moments resisting relative rotations between sites. Two conceptually similar approaches have been proposed to link local interactions to continuum response. In the first one, the local forces are related to the stresses in the continuum cell, e.g. [7,8]. In the second one, the interactions are represented by structural beam elements, the stiffness coefficients of which are determined by equating the strain energy in the discrete and the continuum cell, e.g. [9,10]. In both cases explicit relations between local and continuum parameters can be established for regular lattices. It has been previously shown that regular 3D lattices based on simple cubic, face-centred cubic and hexagonal closely-packed atomic arrangements can be used to represent materials exhibiting cubic elasticity. However, the only isotropic materials such lattices could represent are materials with zero Poisson's ratio [11].

A bi-regular lattice that can represent all materials of practical interest has been proposed recently [12]. It can be seen as a lattice based on body-centred cubic atomic arrangement with two types of links - between neighbours along body diagonals (nearer) and between neighbours along cell edges (further). This lattice, currently formed by beams clamped at sites, is used in the current work together with microstructure data for concrete obtained with X-ray computed tomography. Failure models based on microstructure data and the novel lattice have been previously used for modelling tensile and compressive behaviour of cement [13] and the compressive behaviour of concrete under various complex loading conditions [14]. This work makes a step into developing our understanding of the micro-crack population and its relation to macroscopic damage. Further, the structure of the micro-crack population will provide the means to study the changes in transport properties with damage in future studies.

Most of the work relating micro-crack populations to elastic moduli follows the fundamental paper [15], where analytical statistical derivation of the relation was provided. We follow the interpretation given in [16], in which the damage is measured as a relative change of the elastic modulus and related to micro-crack population via

$$D = 1 - \frac{E}{E(0)} = \frac{\beta}{N_T}\sum_{c\geq 1} c^3 N(c), \tag{1}$$

where c is some measure of micro-crack size, $N(c)$ is the number of micro-cracks of size c, N_T is the total number of sites capable of nucleating micro-cracks, and β is a scaling parameter reported as 0.47π for cracks in a 2D medium. Eq. (1) is our point of comparison for the simulations performed with the lattice model for various loading cases. In the current work we are interested in testing the range of applicability of Eq. (1) and understanding the reasons for deviation from this rule, should such occur, by explicitly analysing the micro-crack population growth. It should be mentioned, that we do not presuppose a value for the scaling parameter β. The simulations are performed with a 3D model and used to derive mechanistically relations between mechanical damage parameters and geometrical characteristics of formed micro-crack populations. The scaling parameter β could be extracted from such relations only for special loading cases as shown in Section 4.

2. Materials and methods

2.1. The site-bond model

The lattice model used in this work is illustrated in Fig. 1. The unit cell, shown in Fig. 1(a) is a truncated octahedron – a solid with

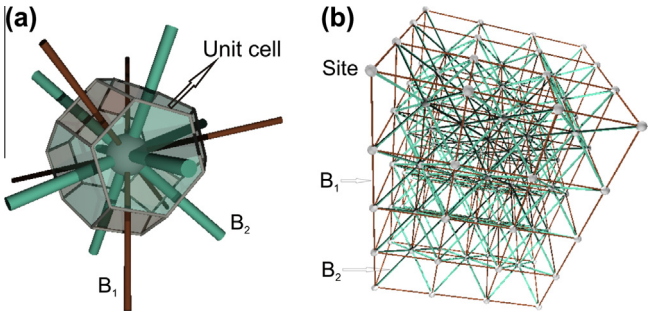

Fig. 1. Lattice illustration: (a) unit cell showing the site with 14 coordinating bonds: six principal, B_1, and eight octahedral, B_2 and (b) discrete lattice of beam elements.

six square and eight regular hexagonal boundaries. The 3D space can be compactly tessellated using such cells, with each cell representing a material microstructure feature, e.g. a block or a grain, in an average sense. This representation is supported by physical and statistical arguments [12]. In brief, the truncated octahedron is topologically closest to the average cell in a random Voronoi subdivision of space. A discrete lattice is formed by placing sites at the centres of the cells and connecting each site to its 14 nearest neighbours; example is shown in Fig. 1(b). The lattice contains two types of bonds. Bonds denoted by B_1 are normal to the square boundaries and form an orthogonal set. For convenience this set is made coincident with the global coordinate system and B_1 are referred to as the principal bonds. Bonds denoted by B_2 are normal to the hexagonal boundaries. The hexagons lie on the octahedral planes with respect to the selected coordinate system, hence B_2 are referred to as the octahedral bonds.

If the spacing between sites in the principal directions is denoted by L, bonds B_1 have length $L_1 = L$, and bonds B_2 have length $L_2 = \sqrt{3}\ L/2$. Presently, the bonds are represented by structural beam elements of circular cross sections, with R_1 and R_2 denoting the radii of beams B_1 and B_2, respectively. The beams are clamped at the lattice sites. The two types of beams have identical Young's modulus, E_b, and Poisson's ratio, ν_b. This reflects the understanding that locally, i.e. at a cell length scale, the material is homogeneous. It has been previously shown [12], that by calibrating four parameters: R_1/L, R_2/L, E_b, and ν_b, the lattice can produce any material with cubic elasticity and with special selections a large class of isotropic elastic materials with Poisson's ratios of practical interest. The reference material in this work is a concrete with $E = 46$ GPa and $\nu = 0.27$, for which the calibration, assuming isotropic elasticity, yields $R_1/L = 0.2$; $R_2/L = 0.32$; $E_b = 90$ GPa; and $\nu_b = 0.4$ [14]. The commercial software Abaqus [17] with Euler–Bernoulli beam formulation has been used for the calibration and the analyses reported in this work.

2.2. Pore distribution and model length scale

Microstructure data for the reference material was obtained using X-ray Computed Tomography as reported in [14]. The pore size distribution was obtained by segmentation of reconstructed 3D images. The studied regions of interest had dimensions of $1700 \times 1200 \times 1200$ voxels with a voxel size of ca. 15 μm, allowing for a minimum detectable pore radius of ca. 15 μm. The number of pores measured experimentally was $n \approx 41{,}500$. The measured pore radii, c_i, were used to construct a cumulative probability distribution (CPD) with standard median ranking, where for pore radii ordered as $c_1 \leqslant c_2 \leqslant \cdots \leqslant c_n$, the cumulative probability for pores with radii less than c_i is given by $F(c < c_i) = (i - 0.3)/(n + 0.4)$. The CPD for the reference material is shown in Fig. 2(a), where the

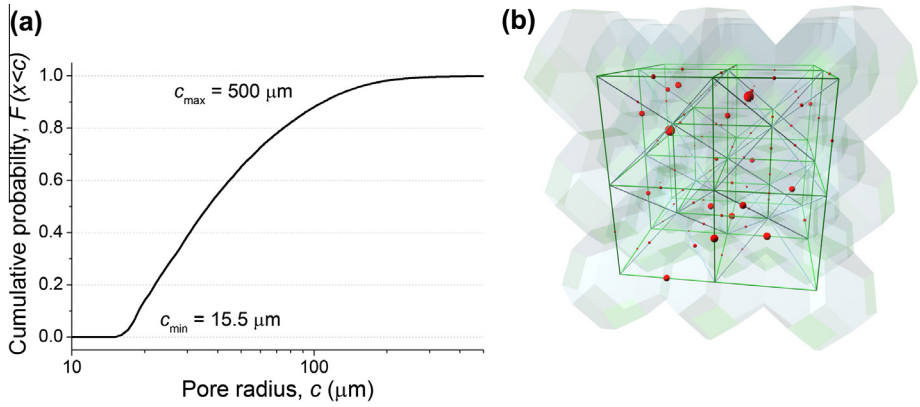

Fig. 2. Pore distribution: (a) cumulative probability of pore radii in the concrete and (b) segment of model illustrating pores distributed to cell boundaries and corresponding. Pore sizes are to scale with the cell size.

minimum and maximum pore radii are also depicted. The CPD is used to assign pore sizes to the lattice bonds. For each bond a uniformly distributed random number $0 \leqslant p < 1$ is generated and the assigned pore radius is calculated from $c = F^{-1}(p)$. This is performed by interpolation between experimental data points for given p. The process ensures that the distribution of pore sizes in the model comes from the same population as in the experiment, a standard statistical argument.

A fragment of the model with distributed pores is given in Fig. 2(b). The cell size, L, is calculated such that the volume of all distributed pores divided by the volume of the cellular structure equals the material porosity. For the reference material the porosity is ca. 5%, which leads to cell sizes in the range 1.8–2.0 mm, depending on the random distribution. The pore sizes shown in Fig. 2(b) are to scale with the sketched cellular structure. With respect to the cellular structure pores reside at cell boundaries. The lattice bonds are also depicted (with radii not to scale) to show that pores reside at bond centres.

2.3. Failure criterion and micro-crack generation

Damage in the lattice model is introduced by removal of bonds. Propensity for bond failure is measured by the parameter

$$\Pi = \frac{N}{N_f} + \frac{|S|}{S_f} + \frac{|T|}{T_f} + \frac{|M|}{M_f}, \tag{2}$$

where N and S are the normal and shear forces in the beam; T and M are the twisting and bending moments; N_f, S_f, T_f, and M_f are critical values. N is positive for tension and negative for compression. S and M are obtained from the values in the two directions normal to the beam axis using the square root of squares rule. Eq. (2) provides an interaction between the different forces that allows for failure when $\Pi \geqslant 1$ under the combined action of normal and shear stresses [14,18]. Taking only the first and fourth term was previously used in criteria with no account for shear, e.g. [19]. The second and third term allow for shear failure similarly to [10].

The failure parameters N_f, S_f, T_f, and M_f can be related [18]. For a beam of circular cross section of radius R, the tensile failure stress is $\sigma_f = N_f/(\pi R2)$. The maximum bending stress is $\sigma_{max} = 4M/(\pi R3)$, which equals σ_f when $M_f = N_f R/4$. Similarly, the shear failure stress is $\tau_f = S_f/(\pi R2)$. The maximum torsion stress is $\tau_{max} = 2T/(\pi R3)$, which equals τ_f when $T_f = S_f R/2$. Thus Π requires two material parameters: σ_f and τ_f. Noting that for quasi-brittle materials typically $1 \leqslant \tau_f/\sigma_f \leqslant 2$ [18], in this work $\tau_f = 2\sigma f$ is used, representing more brittle materials.

The tensile failure strength of a bond, σ_f, is related to the size of the pore assigned to the bond. The relation used here is simpler than in the previous work [14] and based on the assumption that σ_f is the beam remote stress for which the average stress in the beam ligament outside the pore attains a critical value σ_0. Thus

$$\sigma_f = \sigma_0 \left[1 - \left(\frac{c}{R}\right)^2\right], \tag{3}$$

where c and R are the pore and beam radii, respectively, and σ_0 can be interpreted as the tensile strength of the material without a defect. With this setup and the choice $\tau_f = 2\sigma_f$ the failure model requires a calibration of a single parameter, σ_0, against experimental stress–strain curve. However, since the beams behaviour is linear elastic, the choice of σ_0 would affect only the calculated macroscopic stresses but not the order in which damage (beam failures) would evolve in the system. Because the interest here is investigating the evolution of damage, $\sigma_0 = 1$ MPa is used for the calculations, noting that macroscopic stress response can be simply scaled by another value of σ_0. Note, that the sizes of the distributed pores affect the failure stresses of individual bonds via Eq. (3), hence each bond has a different propensity for failure calculated by Eq. (1).

Table 1
Boundary conditions for loading cases: values given in bold denote applied conditions; A stands for values obtained from finite element analyses.

Case	U_1	U_2	U_3	F_1	F_2	F_3	Note
C1	$\boldsymbol{d_1}$	A	A	A	**0**	**0**	Uniaxial unconfined extension
C2	$\boldsymbol{d_2}$	$\boldsymbol{d_2}$	A	A	A	**0**	Plane stress
C3	$\boldsymbol{d_3}$	$\boldsymbol{d_3}$	**0**	A	A	A	Plane strain
C4	$\boldsymbol{d_4}$	**0**	**0**	A	A	A	Uniaxial confined extension

3. Calculations

3.1. Lattice geometry and boundary conditions

A model of size ($20L$, $20L$, $20L$) was used for numerical simulations. The lattice contained 17,261 sites and 113,260 bonds: 49,260 B_1 and 64,000 B_2. The global coordinate system (X_1, X_2, X_3) was coincident with bonds B_1, so that the boundary planes $X_1 = 0$, $X_1 = 20L$, $X_2 = 0$, $X_2 = 20L$, $X_3 = 0$, $X_3 = 20L$ contained 21×21 sites (nodes). Boundary conditions were applied via prescribed displacements of nodes on boundary planes. Only displacements normal to a plane were applied to its nodes, while other displacements and rotations were unconstrained. Therefore the only non-zero reaction forces at nodes were those normal to their plane. The displacements and forces of nodes on a plane with normal X_i are denoted by U_i and F_i. Table 1 shows the conditions on planes $X_1 = 20L$,

$X_2 = 20L$, and $X_3 = 20L$ for the analysed cases. Additionally, $U_1 = 0$ on $X_1 = 0$; $U_2 = 0$ on $X_2 = 0$; $U_3 = 0$ on $X_3 = 0$, apply to all.

For cases where nodal reaction forces were determined from analysis, the macroscopic stress in the respective direction was calculated as the ratio between the total reaction force and the boundary area, i.e. $\sigma_i = \Sigma F_i/400L^2$. For the cases where nodal displacements were determined from analysis, the macroscopic strain in the respective direction was calculated as the ratio between the average displacement and the model length, i.e. $\varepsilon_i = \Sigma U_i/(21^2 \times 20L)$.

3.2. Bond failure and damage recording

The evolution of damage was simulated by failure of bonds, controlled by an in-house code, and repetitive solution for equilibrium performed by Abaqus with constant applied displacements. The values of $\boldsymbol{d_i}$ were selected so that the strain energy density in the system prior to damage was one for the four cases for the purpose of comparison. At each step the in-house code obtains the forces and moments in all bonds and calculates the propensity for failure, Π, for each bond. The bond with maximum Π is then removed and the updated lattice is solved for equilibrium. This leads to redistribution of forces for the continuous damage evolution.

The magnitudes of Π at which consecutive failures occurred can be used to cut-back the applied strain and resulting stress and obtain a macroscopic stress–strain response. For a selected physically based tensile strength, σ_0, and a given load, the propensities for failure of the bonds can be ordered by decreasing magnitude. Since the problem is elastic the applied load can be arbitrary. The bond with the highest propensity will determine the load level at which this bond would fail, while all other bonds would remain intact. The macroscopic stress and strain at this load level provide a point on the stress–strain curve. The full curve is then constructed from the points corresponding to the individual failure events. Details of the process and resulting curves for uniaxial loadings can be found in [14,19]. It should be mentioned that this construction can also be used for complex loadings, but the response curves that can be constructed would relate stress tensor invariants to strain tensor invariants. Since the focus of this work is on the relation between damage and crack population, the construction of stress–strain behaviour curves is not necessary and we use an arbitrary tensile strength, σ_0. For the study we define four damage parameters, measuring the relative changes of the hydrostatic stress and the three components of the stress deviator by:

$$D_H = 1 - \frac{\sigma_H}{\sigma_H(0)} \tag{4a}$$

$$D_i = 1 - \frac{S_i}{S_i(0)}, \quad \text{where } S_i = \sigma_i - \sigma_H,\ i = 1,2,3 \tag{4b}$$

It is straightforward to see that these parameters must remain equal when the deformation and damage of the material are isotropic. In such cases the definitions are also equivalent to the damage parameter defined via relative reduction of Young's modulus or shear modulus, such as the one used in Eq. (1).

3.3. Crack population analysis

A bond failure is thought of as a micro-crack nucleation, specifically as a separation between the adjacent cells in the cellular structure along their common face. Initially, the micro-cracks may be dispersed in the model reflecting the random distribution of pore sizes and the low level of interaction due to force redistribution. Interaction and coalescence may follow as the population of micro-cracks increases. These situations are illustrated in Fig. 3. The structure of the failed surface can be represented with a mathematical graph, where graph nodes represent failed faces and graph edges exist between failed faces with common triple line in the cellular structure, i.e. where two micro-cracks formed a continuous larger crack. With reference to Fig. 3, each failed face is a graph node and each pair of neighbouring failed faces is a graph edge.

Generally, the graph of a failed surface is a disconnected set of sub-graphs or components, some of which could be single nodes as at the start of damage evolution, Fig. 3(a), while others could be connected sets representing larger micro-cracks as the coalescence develops, e.g. the connected micro-crack in Fig. 3(b). For the analysis, nodes are equipped with weights equal to the failed face areas. Edges are equipped with weights equal to the shortest path along connected faces between their centres. Hence, the graph representing the entire failed surface contains a number (possibly zero) of isolated nodes (micro-cracks of one failed face); a number (possibly zero) of sub-graphs with two nodes and one edge (micro-cracks of two neighbouring failed faces); and so on until the largest sub-graph in terms of connected nodes (failed faces).

The components of a failed surface graph are sorted into sets according to their areas $A_1 < A_2 \ldots < A_k$, so that each set contains N_i disconnected components of area A_i. The linear size of a component is approximated with the square root of its area so that the moment of the crack population is formed using (compare to Eq. (1))

$$M = \frac{1}{A_T}\sum_{i=1}^{k} A_i^{3/2} N_i, \tag{5}$$

where A_T is the total area of the faces in the cellular structure. This can in principle be replaced with a linear measure to conform to Eq. (1). A realistic choice is to use the component diameter which is the maximal shortest path between component's nodes calculated with the weighted edges. The process, however, is computationally expensive and does not lead to noticeable changes in the results for the cases analysed here. Eq. (5) is used after each failure event to calculate the evolution of the moment with damage. In addition, the maximal component is monitored. This is the largest connected cracked surface.

4. Results and discussion

4.1. Damage induced anisotropy

Fig. 4 shows the results of the evolution of the damage parameters defined by Eq. (4) as functions of the moment of crack population defined by Eq. (5). Recall that a damage parameter, based on the relative change of the Young's modulus equals the damage parameters based on the individual stress components, deviatoric and hydrostatic, when the material remains macroscopically isotropic. In this case the same damage parameter describes the relative change of the shear modulus. The results for the cases of uniaxial extension, unconfined (a) and confined (d), show equality of the four damage parameters (approximate in case 4). This suggests that microscopic isotropy is maintained during damage evolution and the results reproduce very closely the linear relation predicted by the theory and given by Eq. (1). Notably, an estimate for the slope of the linear function from the figures is about 1.5, which is very close to the value of β reported in relation to Eq. (1) [16]. Hence, the relation between damage and micro-crack population descriptor in 3D under the special cases of uniaxial tension (a) and uniaxial extension (d) is practically equivalent to the analytical result for 2D.

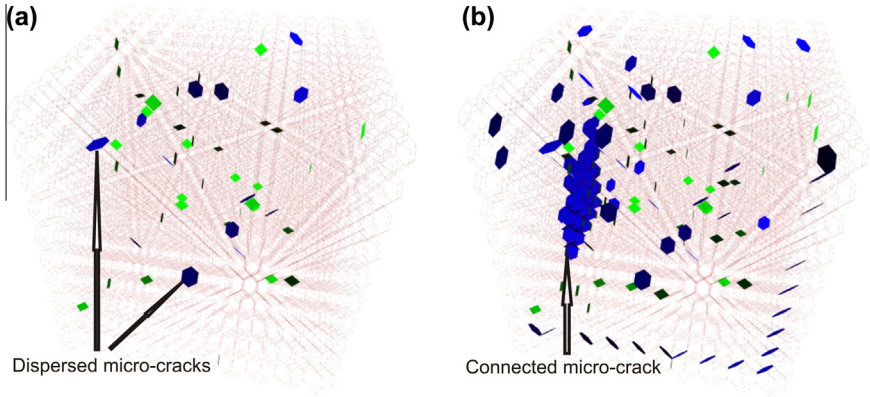

Fig. 3. Illustration of micro-crack populations, presented as failed faces between cells: (a) dispersed population, characterised by predominantly separated individual failures, typical for initial stages of damage evolution and (b) population of disconnected micro-cracks of different sizes, typical for later stages of damage. Underlying cellular structure is shown as a background; failed faces are shown with their geometrical shape, either square or hexagon.

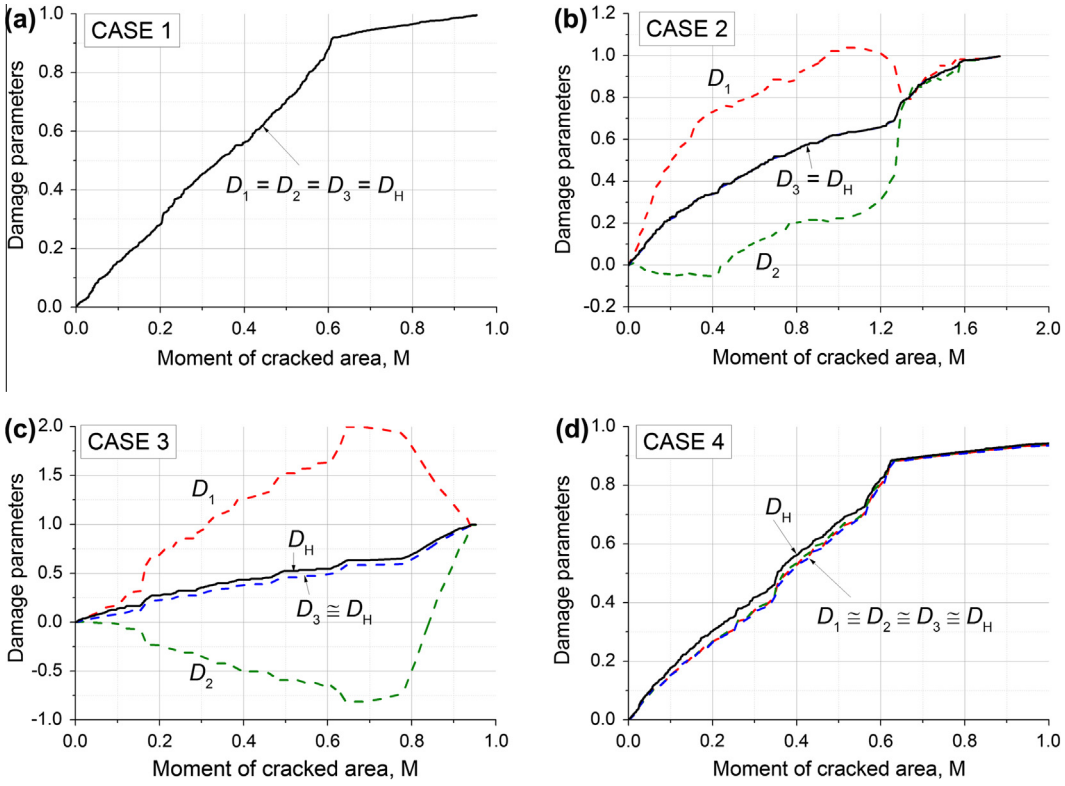

Fig. 4. Damage parameters relation to crack population moment.

In the cases of plane stress (b) and plain strain (c), however, the development of damage is radically different, illustrating the development of damage-induced anisotropy. In this case the damage parameter D_i represents the relative reduction of the longitudinal shear modulus in direction X_i. Note, that this is not the shear modulus relating shear stress to shear strain. Considering the definition given by Eq. (4b), a damage parameter larger than one indicates negative resistance to shear in a particular direction, i.e. the resistance shifted from the initial positive to a negative value as the micro-crack population evolved. Inversely, a damage parameter smaller than zero indicates a resistance to shear larger than the initial one, i.e. the micro-crack population evolution increased the shear resistance of the material in the corresponding direction. In both plane cases, the evolution of D_1 suggest that the system undergoes transition into negative longitudinal shear resistance, quite more pronounces in the plane strain case (c), while the shear resistance in direction X_2 increases from its initial value.

Negative shear resistance is not unusual for anisotropic materials. The bounds for Poisson's ratios in such materials calculated in [20,21] allow for negative longitudinal shear moduli with the values recorded here. The thermodynamic stability of the system when one of the longitudinal shear moduli is decreasing is ensured by the increase of the other longitudinal shear modulus. The results merely show that extreme anisotropy has been developed in the material with the evolution of micro-crack population under the two plane cases. The development of the hydrostatic damage is also affected in these cases, as it cannot be described as a linear function of the cracked area moment. The mechanical damage in

this case cannot be measured by a single parameter hence the plots are against a measurable characteristic of the micro-crack population.

4.2. Maximal graph component (main crack) structure

To understand what causes the anisotropy in the plane cases the structure of the crack population needs to be studied in more detail. This requires a single damage parameter; an appropriate choice is the relative reduction of the strain energy density in the system, $D = 1 - W/W(0)$, which is found to be approximately equal to the damage parameter defined via the relative reduction of the hydrostatic stress in all cases, see Fig. 5(a).

The development of the maximal graph component, i.e. the main crack, with damage is shown in Fig. 5(b) with the ratio between the area of the maximal component, A_m, to the total cracked area, A. It is clear that the main crack becomes dominant very early in the development of damage (at damage less than 1%) and its relative area grows nearly exponentially for all cases. It seems therefore sufficient to examine the structure of the maximal component as the damage develops.

Fig. 6 shows the development of the maximal component area, split into the areas of surfaces normal to the three principal axes, A_1, A_2, A_3, and the surfaces formed on octahedral planes, A_4. All areas are normalised with the total areas of the corresponding boundaries in the cellular structure. In the cases of uniaxial extension, unconfined (a) and confined (d), the development of the main crack involves creation of surfaces normal to the applied load and on octahedral planes. Although there is a difference between the two cases in the rates of creation of normal and octahedral surfaces, the overall balance results in isotropic damage, see Fig. 4(a and d).

In the plane stress (b) and plane strain (c) cases, the development of the main crack follows very different patterns. The parallel increase of normal to the first loading axis and octahedral surfaces in plane stress, Fig. 6(b), seems to be responsible for the immediate development of damage-induced anisotropy, which after that appears to be moderated by the development of surfaces normal to the second loading axis. The constraint in plane strain, Fig. 6(c), leads to a delayed but rapid increase of surfaces normal to the first loading axis together with a lower rate of creation of octahedral surfaces. This appears to delay substantially the development of cracked surfaces normal to the second loading axis and results in significantly higher anisotropy.

It should be noted that the structure-damage relations reported here were found qualitatively independent of the random assignment of pores in the lattice model as well as of the shape parameter of the pore distribution. This has been confirmed by a number of simulations with different shape of distribution and random assignments. One parameter that may affect the outcomes is the shear to normal strength ratio; this is a subject of ongoing work. It is further understood that the outcomes reported here are principally related to the selected lattice connectivity. However, the detail to which the fracture surface topography can be studied with the proposed model is higher than the detail allowed by previous models based on cubic lattices. One unknown in the analysis is whether the crack development in the lattice is energetically equivalent to the development of continuous cracks. This question remains to be addressed in a future work.

The current observations suggest that a common, constraint independent, damage evolution law might not be feasible to achieve. In such case it seems that a lattice-based analysis might be necessary as a sub-modelling approach to inform the behaviour of finite elements in a continuum model. However, if a damage evolution law can be derived from simulations of this kind, it is clear than it must depend on the three invariants of the stress tensor. *This observation challenges the use of damage evolution laws based on a single damage parameter for loads different from uniaxial extensions.*

4.3. Is global failure a weakest-link event?

The last question of interest in this work is related to the use of the weakest-link statistics for global failure predictions. It was suggested in [16] that weakest-link should be applied to the population of micro-cracks in the system. However, from the simulations performed here it is evident that a single crack, the maximal connected component of the cracked surface, becomes rapidly dominating the behaviour, Fig. 5(b), with few much smaller components disconnected from the main crack. This does not allow for invoking the weakest-link, because the interactions between micro-cracks via load redistribution cannot be captured by extreme-value statistics.

Another approach would be to base the weakest-link statistics on the microstructure information, in this case the size distribution of crack-initiation features, the pores. This is similar to the approach used in the modelling of cleavage fracture, where second-phase particles are considered to be cleavage initiators. In order to show whether this is a realistic approach, a comparison is made between the probability density of pore sizes distributed in the lattice and pore sizes contained in the maximal component at failure. The results are shown in Fig. 7 for the pores in the entire lattice (a) and three of the loading cases as depicted. The results shown correspond to one and the same random assignment of pore sizes.

Evidently, the probability density of the pores belonging to the final fracture surface is different from the lattice distribution and depends on the loading mode. While the initial damage may start

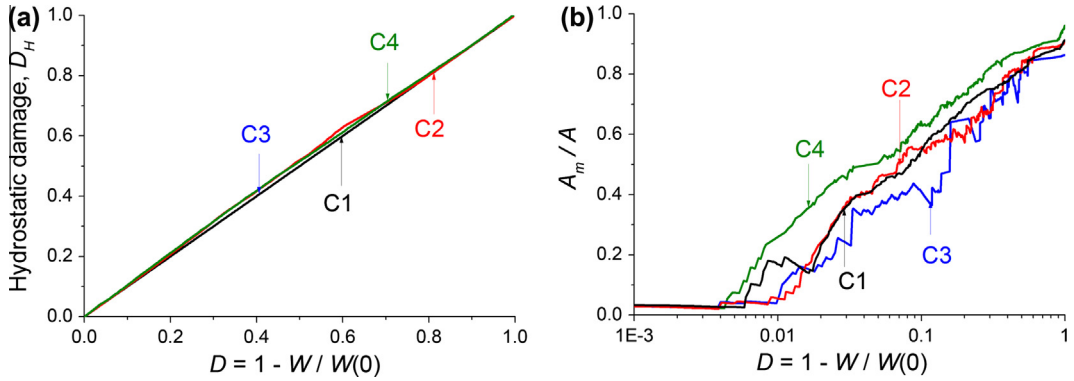

Fig. 5. Hydrostatic damage (a) and relative area of main crack (b) development with damage defined as relative reduction of strain energy density.

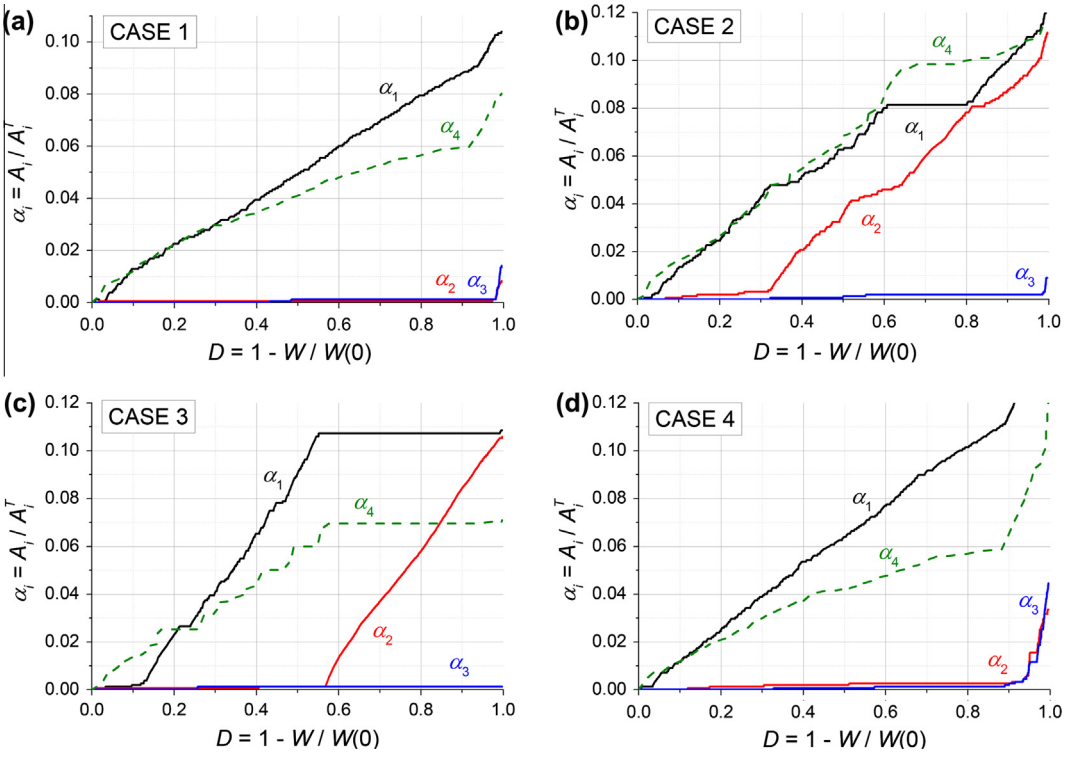

Fig. 6. Structure of maximal graph component with damage.

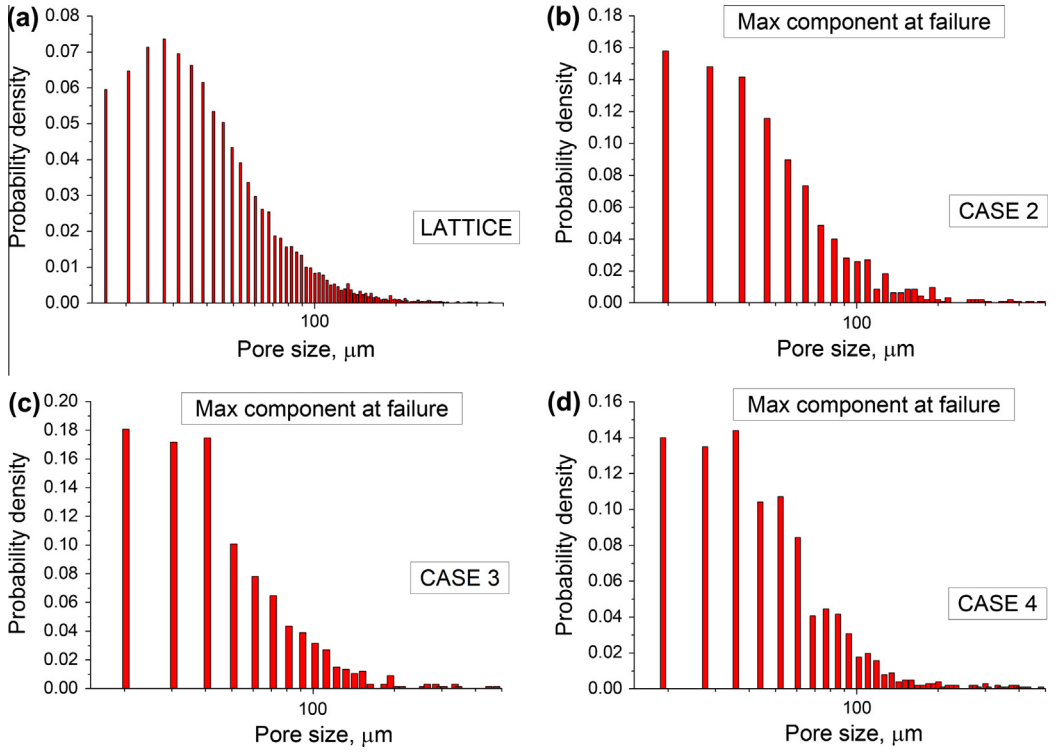

Fig. 7. Probability density of pore sizes in the lattice (a) and in the maximal component at failure for three loading cases (b–d). Results obtained with the same distribution given by (a).

at one and the same location in the system, the nature of loading develops the main crack in different ways and the final failure cannot be described as a weakest-link event using the statistics of the sizes of the failure initiation sites. This makes it difficult to derive a load-independent, purely microstructure based relation between the macroscopic damage and the probability of failure. *The outcome challenges the use of the weakest-link statistics for assessing global failure.* It supports further the suggestion that macroscopic failure analysis needs to be performed with an underlying lattice-based analysis of local micro-crack propagation.

4.4. Model and method discussion

The proposed model uses structural beam elements to represent interactions between sites (material blocks). While this is in line with many previous works, e.g. [9,10,19], the formulation introduces a relation between forces and moments governed by the implemented beam theory. This is a limitation of the model from the solid mechanics perspective. In a more general case, the interactions between sites should be represented by bundles of six spring-like elements, resisting independently the relative translations and rotations between sites [11]. In such case, the lattice would represent a generalised continuum with independent translational and rotational degrees of freedom and would require the calibration of one additional material parameter (in the isotropic case), called coupled-stress constant [22]. Closed form relations between the translational spring constants and the classical macroscopic elastic properties have already been obtained, using the energy equivalence approach in [11], and reported in [23]. These have been successfully used for modelling damage evolution in nuclear graphite with no account for rotations [24]. The rotational spring constants, however, require the knowledge of the coupled-stress constant of the material which depends on the sizes of and the distances between the microstructure features at lattice sites. Experimental and analytical work is ongoing to establish methodology for calculation of the coupled-stress constant for given microstructure.

The purpose and strength of the proposed model is to provide the link between the specific microstructure features and the emergent macroscopic mechanical response. This is in addition to the natural way with which micro-crack generation, interaction, growth and coalescence are analysed, with no reliance on constitutive assumptions for these processes. Generally, the microstructure features that can be accounted for in the model are of two types: (1) features determining lattice cells and residing at lattice sites, e.g. concrete aggregates or rock blocks and (2) features capable of micro-crack initiation residing at lattice cell boundaries, e.g. pores or existing fractures. Such a methodology has been used in a work related to nuclear graphite [25]. In this work the site features have not been explicitly accounted for, which is presently a limitation to the physical realism of the microstructure representation. Their length scale has not been used in the model construction to derive the model length scale L. Instead, the model length scale has been determined entirely from the material porosity and the assumption that the micro-crack initiating features are present on all boundaries of the cellular lattice. The reason for this is the lack of experimental data for site features' sizes and volume density, or alternatively statistics of distances between them, in the study material. With such data, the model length scale will be more physically based, e.g. on the average distance between site features or on the distribution of sizes and volume density of features. The assignment of micro-crack initiating features to boundaries would then be performed either to a fraction of the cell boundaries or to all with multiple defects in some boundaries, depending on the material porosity. Experimental and modelling work is ongoing for the determination of all microstructure parameters for more realistic model construction. This will be reported in a future publication.

The loading cases analysed in the work have been selected for two reasons. Firstly, to examine the relation between micro-crack size population and damage evolution previously derived [15,16]. Secondly, to study the behaviour of a volume element ahead of a macroscopic crack, where plane stress and plane strain conditions prevail towards the ends and the middle section of the crack front, respectively. The latter is in view of a future development of microstructure-informed mechanistic methodology for the assessment of integrity of quasi-brittle materials containing macroscopic flaws (cracks, fractures). Such a methodology can be based either on coupled models for material behaviour, involving damage evolution laws, e.g. [26], or on uncoupled models based on the statistical size distribution of failure initiating features, e.g. [27]. In the former case, the stability or growth of a macroscopic flow is determined by the changing material properties as damage ahead of the flow evolves. The results in this work suggest that the damage evolution law for coupled models must depend on three invariants of the stress tensor in the general case. This is of particular importance in geomechanics, where the stress fields are either biaxial on surface or triaxial in depth. In the case of uncoupled models, the results of this work suggest that the widely used weakest-link statistics for global failure assessment [27] cannot be safely applied on the basis of measured size distribution of micro-crack initiating features. It seems that the development of new coupled models for quasi-brittle media, specifically microstructure-informed damage evolution laws, would be the more rewarding way ahead. The four loading cases considered in the work need to be complemented by analyses of a range of triaxiality conditions. This is a subject of ongoing work for selected microstructures. Potential limitation of the approach is that each particular microstructure would require separate analyses for sufficient number of stress triaxiality conditions to derive a macroscopic damage evolution law. This could be overcome by incorporating the proposed methodology as a sub-model to continuum finite element models, with lattice covering one element or a region of elements as required by the element size and the microstructure length.

An additional strength of the proposed methodology is the explicit analysis of the connected components of the fractured surface. These provide the easy pathways for transport through the porous/fractured medium and can be naturally represented by pore networks with appropriate local transport coefficients. Thus the evolution of damage can be complemented by pore space models, e.g. [28,29], to analyse the resulting evolution of the medium transport properties. Coupled mechanical-transport models informed by the microstructure are currently being developed for applications in the safety analysis of engineered barriers in nuclear waste disposal facilities, and in the area of hydrocarbon recovery with hydraulic fracturing.

5. Conclusions

It was demonstrated that in cases of non-uniaxial extension, such as plane stress or plane strain found ahead of a main crack, the micro-crack population development was responsible for elastic anisotropy with extreme variations of longitudinal shear moduli.

It was shown that the damage-induced anisotropy was a complex function of the crack population structure. A load-independent damage evolution law might not be achievable and explicit analysis of crack population development, e.g. using a lattice model, might be necessary to complement continuum finite element analysis of failure.

It was shown that the maximal connected component of the crack population, i.e. the largest crack, became dominant very early in the process of macroscopic damage and controlled the ultimate failure. The analysis if this component suggested that the global failure could not be treated as a weakest-link event.

The graph-theoretical approach to the analysis of micro-crack populations showed significant potential to reveal the underlying topological structure of the cracked surface. Further work is required to link the topological structure to a measure for global probability of failure, or develop microstructure-informed damage evolution laws.

The analysis of micro-crack populations allows for the natural construction of discrete transport models, with which to study

the changes of macroscopic transport coefficients, e.g. permeability or diffusivity, with the development of damage.

Acknowledgments

The author acknowledges the support from EPSRC via grant EP/J019763/1, "QUBE: Quasi-Brittle fracture: a 3D experimentally-validated approach", and from BNFL for the Research Centre for Radwaste & Decommissioning.

References

[1] G. Pijaudier-Cabot, Z.P. Bazant, Nonlocal damage theory, J. Eng. Mech. 113 (1987) 1512–1533.
[2] J.W. Ju, On energy-based coupled elastoplastic damage theories: constitutive modelling and computational aspects, Int. J. Solids Struct. 25 (1989) 803–833.
[3] P. Grassl, M. Jirasek, Damage-plastic model for concrete failure, Int. J. Solids Struct. 43 (2006) 7166–7196.
[4] J. Cervenka, V. Papanikolaou, Three dimensional combined fracture-plastic material model for concrete, Int. J. Plasticity 24 (2008) 2192–2220.
[5] H.S. Wong, M. Zobel, N.R. Buenfeld, R.W. Zimmerman, Influence of the interfacial transition zone and microcracking on the diffusivity, permeability and sorptivity of cement-based materials after drying, Mag. Concr. Res. 61 (2009) 571–589.
[6] K.L. Scrivener, A.K. Crumbie, P. Laugesen, The interfacial transition zone (ITZ) between cement paste and aggregate in concrete, Interface Sci. 12 (2004) 411–421.
[7] Z.P. Bazant, B.H. Oh, Microplane model for progressive fracture of concrete and rock, J. Eng. Mech. 111 (1985) 559–582.
[8] G. Cusatis, Z.P. Bazant, L. Cedolin, Confinement-shear lattice CSL model for fracture propagation in concrete, Comp. Meth. Appl. Mech. Eng. 195 (2006) 7154–7171.
[9] D.V. Griffiths, G.G.W. Mustoe, Modelling of elastic continua using a grillage of structural elements based on discrete element concepts, Int. J. Numer. Meth. Eng. 50 (2001) 1759–1775.
[10] C.S. Chang, T.K. Wang, L.J. Sluys, J.G.M. van Mier, Fracture modeling using a micro structural mechanics approach – I. Theory and formulation, Eng. Fract. Mech. 69 (2002) 1941–1958.
[11] Y. Wang, P. Mora, Macroscopic elastic properties of regular lattices, J. Mech. Phys. Solids 56 (2008) 3459–3474.
[12] A.P. Jivkov, J.R. Yates, Elastic behaviour of a regular lattice for meso-scale modelling of solids, Int. J. Solids Struct. 49 (2012) 3089–3099.
[13] A.P. Jivkov, M. Gunther, K.P. Travis, Site-bond modelling of porous quasi-brittle media, Mineral. Mag. 76 (2012) 2969–2974.
[14] A.P. Jivkov, D.L. Engelberg, R. Stein, M. Petkovski, Pore space and brittle damage evolution in concrete, Eng. Fract. Mech. 110 (2013) 378–395.
[15] B. Budiansky, R.J. O'Connell, Elastic moduli of a cracked solid, Int. J. Solids Struct. 12 (1976) 81–97.
[16] W.A. Curtin, H. Scher, Time-dependent damage evolution and failure in materials. I. Theory, Phys. Rev. B 55 (1997) 12038–12050.
[17] ABAQUS 6.11, DS Simulia Corp., 2011.
[18] Y. Wang, S. Abe, S. Latham, P. Mora, Implementation of particle-scale rotation in the 3D-lattice solid model, Pure Appl. Geophys. 163 (2006) 1769–1785.
[19] E. Schlangen, J.G. M van Mier, Experimental and numerical analysis of micromechanisms of fracture of cement-based composites, Cem. Concr. Compos. 14 (1992) 105–118.
[20] A.N. Norris, Extreme values of Poisson's ratio and other engineering moduli in anisotropic materials, J. Mech. Mater. Struct. 1 (2006) 793–812.
[21] C.Y. Guo, L.T. Wheeler, Extreme Lamé compliance in anisotropic crystals, Mater. Mech. Solids 14 (2009) 403–420.
[22] A.R. Hadjesfandiari, G.F. Dargush, Couple stress theory for solids, Int. J. Solids Struct. 48 (2011) 2496–2510.
[23] M. Zhang, C.N. Morrison, A.P. Jivkov, A meso-scale site-bond model for elasticity: theory and calibration, Mater. Res. Innov., in press. (2014), http://dx.doi.org/10.1179/1432891714Z.000000000537.
[24] C.N. Morrison, A.P. Jivkov, G. Smith, J.R. Yates, Lattice-spring modelling of graphite accounting for pore size distribution, Key Eng. Mater. 592–593 (2014) 92–95.
[25] C.N. Morrison, M. Zhang, A.P. Jivkov, J.R. Yates, A discrete lattice model of quasi-brittle fracture in porous graphite, Mater. Perform Char., in press. (2014), http://dx.doi.org/10.1520/MPC20130077.
[26] V. Tvergaard, A. Needleman, Analysis of the cup-cone fracture in a round tensile bar, Acta Metal. 32 (1984) 157–169.
[27] F.M. Beremin, A local criterion for cleavage fracture of a nuclear pressure vessel steel, Metal. Trans. A 14 (1983) 2277–2287.
[28] A.P. Jivkov, C. Hollis, F. Etiese, P.J. Withers, A novel architecture for pore network modelling with applications to permeability of porous media, J. Hydrol. 486 (2013) 246–258.
[29] Q. Xiong, A.P. Jivkov, J.R. Yates, Discrete modelling of contaminant diffusion in porous medium with limited microstructure information, Micropor. Mesopor. Mater. 185 (2014) 51–60.